Composite Analysis of Aerosol Direct Radiative Effects on Meteorology During Wintertime Severe Haze Events in the North China Plain

Yucheng Gao[1], Hong Liao[1], Haishan Chen[2,3], Bin Zhu[3], Jianlin Hu[1], Xinlei Ge[1], Lei Chen[1], and Jiandong Li[1]

[1]Jiangsu Key Laboratory of Atmospheric Monitoring and Pollution Control, Collaborative Innovation Center of Atmospheric Environment and Equipment Technology, School of Environmental Science and Engineering, Nanjing University of Information Science & Technology, Nanjing, China, [2]Key Laboratory of Meteorological Disaster, Ministry of Education(KLME)/Joint International Research Laboratory of Climate and Evironment Change(ILCEC), Nanjing University of Information Science & Technology, Nanjing, China, [3]Collaborative Innovation Center on Forecast and Evaluation of Meteorological Disasters (CIC-FEMD), Nanjing University of Information Science & Technology, Nanjing, China

Abstract Previous studies on the impacts of severe haze episode on meteorology were generally focused on single episodes. This study aimed to obtain the common features of the influence of aerosol direct radiative effects on meteorology during severe particulate pollution events by composite analyses on model results from the Weather Research and Forecasting Model with online chemistry. Five heavily polluted events (15–17 January 2014, 13–15 January 2015, 8–10 December 2015, 21–23 December 2015, and 29–31 December 2016) in the North China Plain (NCP, 35.4–41.2°N, 113.3–119.3°E) were selected, which were representative of the most frequently observed weather patterns for severe haze. Model results showed that aerosols in the five heavily polluted events led to strong negative changes in radiative flux of 52.1–86.7 W m^{-2}, reductions in the 2-m temperature by 0.28–0.97°C, and the reductions in planetary boundary layer heights by 23.1–58.5 m, when averaged over the areas with $PM_{2.5}$ concentrations >150 μg m^{-3}. The magnitudes of aerosol induced changes in the 2-m temperature were found to be influenced not only by aerosol concentration but also by wind speed, wind direction, and the convergence or divergence of winds. High wind speed diluted the aerosol-induced cooling, the convergence of wind limited the temperature change to local area, and the intrusion of cold air mass near the surface enhanced the aerosol-induced cooling. In all the cases, aerosols induced an anti-cyclone at 500 hPa around NCP and anomalous northerlies or northeasterlies at the surface in the eastern NCP.

Plain Language Summary The impact of aerosol direct radiative effects (DRE) on meteorology are very important, but previous studies on such effects were generally focused on one pollution episode. In order to obtain the common features of the DRE of aerosols on meteorology, we applied the Weather Research and Forecasting-Chemistry model to simulate five heavily polluted events belonging to the most frequently observed weather patterns for severe particulate pollution in the North China. We found that aerosols lead to the reductions in surface radiative flux, 2-m temperature, and planetary boundary layer height. In addition, the magnitudes of aerosol-induced decreases in 2-m temperature are influenced by winds, including wind speed, wind direction, and the convergence or divergence of winds. High wind speed dilutes the aerosol-induced cooling, the convergence of wind limits the temperature change to local area, and the intrusion of cold air mass near the surface enhances the aerosol-induced cooling. Aerosols also can induce an anti-cyclone at 500 hPa around North China Plain (NCP) and anomalous northerlies or northeasterlies at the surface in the eastern NCP.

1. Introduction

The fast development of China's economy in recent decades was accompanied with frequent occurrence of severe air pollution events in the North China Plain (NCP). Observations revealed that NCP had the highest numbers of severe particulate pollution days (SPPDs, the days with observed daily averaged $PM_{2.5}$ concentrations larger than 150 μg m^{-3}) in China, which were 122, 95, 57, 78, and 31 days in 2013, 2014, 2015, 2016, and 2017, respectively (Li et al., 2019). SPPDs in NCP occurred mostly from November to February of each year. The maximum hourly averaged $PM_{2.5}$ concentrations in NCP reached 680 μg m^{-3} during 9–16 January 2013 (Wang et al., 2013). Even during the lockdown of COVID-19 (from 24 January to 15 February 2020) with significant reductions in social-economic activities (anthropogenic emissions) over China, the maximum $PM_{2.5}$ level reached about

200 µg m^{-3} in Beijing (Li et al., 2021). These high concentrations of pollutants are not only detrimental to human health, but also have large impacts on meteorology (Liao, Lou et al., 2015).

Severe particulate pollution events in China generally occur under stagnant synoptic conditions including weak surface wind, low planetary boundary layer, and high relative humidity (Cai et al., 2017), which are associated with different weather patterns (Zhang et al., 2016). Hou et al. (2019) carried out the obliquely rotated principal component analysis in the T-model (T-PCA) by using sea level pressure (SLP) and 10-m wind, and classified all wintertime days during December 2013 to November 2018 into 4 weather patterns. For each of the four weather patterns, they reported the occurrence frequencies of light (75–115 µg m^{-3}), moderate (115–150 µg m^{-3}), and severe (>150 µg m^{-3}) fine particle pollution. They found that SPPDs over Beijing-Tianjin-Hebei (BTH) mainly occurred under two types of weather patterns that were responsible for 69.5% of the observed SPPDs. Li et al. (2019) selected firstly SPPDs (PM$_{2.5}$ > 150 µg m^{-3}) during April 2013–February 2018 based on observations, and then classified these SPPDs into five types of weather conditions based on the T-PCA analysis by using geopotential height (HGT) at 500 hPa and 850 hPa as well as SLP obtained from the ERA-Interim. They reported that five weather types were responsible for 35.7%, 31.2%, 16.6%, 12.1%, and 4.4% of the observed SPPDs, respectively. Few previous studies examined aerosol radiative effect (ARE) on meteorology under different weather patterns during severe haze events. We present such a study considering the most dominant two weather types from Li et al. (2019).

Previous studies have concluded that ARE influences meteorology during severe haze events. Atmospheric aerosols absorb and scatter solar radiation (direct radiative effect, DRE) or serve as cloud condensation nuclei, changing the microphysical processes of clouds and precipitation (indirect radiative effect, IRE) (Gao et al., 2021). Table 1 summarizes the previous observational studies that reported ARE in NCP during severe haze events. By using the ground-based sunphotometer measurements in the NCP during 10–16 January 2013, Che et al. (2014) revealed that the highest daily mean ARE at the surface over three sites in Beijing reached −200 W m^{-2}, corresponding to the maximum PM$_{2.5}$ level of 520 µg m^{-3}. Based on solar- and sky-scanning radiometer measurements in the NCP during 15–22 December 2016, Zheng, Che, Xia, et al. (2017) reported that the maximum changes in radiative flux at the ground were −227, −199, and −191 W m^{-2} in Beijing, Shijiazhuang, and Jiaozuo, respectively, when the maximum PM$_{2.5}$ concentrations reached about 416, 676, and 677 µg m^{-3}, respectively. Such large reductions in radiative flux were also reported by Bi et al. (2014), Yu et al. (2016), Zheng, Che, Yang, et al. (2017), and Liu et al. (2019) (Table 1).

Online-coupled meteorology-chemistry models have also been used to assess the influence of ARE on meteorology during severe pollution events, as summarized in Table 2. Gao et al. (2015) used the Weather Research and Forecasting-Chemistry (WRF-Chem) model to study a severe particulate pollution event in BTH (36.2–41°N, 114–118°E), and found that ARE (DRE + IRE) of aerosols led to a maximum reduction in surface radiative flux of 140 W m^{-2} and a corresponding reduction in surface temperature of 2.8°C averaged over 09:00–18:00 of 10–15 January 2013 over BTH. Liu et al. (2018) applied the WRF-Chem model and reported that, averaged over NCP and over 18–21 December 2016, aerosol DRE led to perturbations in shortwave radiation and temperature by −69 W m^{-2} and −0.7°C, respectively, when concentration of PM$_{2.5}$ was 310 µg m^{-3}. Wu et al. (2019) used the WRF-Chem model and found that aerosol DRE led to a maximum reduction in surface radiative flux of 180 W m^{-2} and a maximum reduction in surface air temperature of 3.2°C, when averaged over the polluted areas with PM$_{2.5}$ >150 µg m^{-3} during the pollution episode in NCP from 5 December 2015 to 4 January 2016. Studies summarized in Table 2 were generally focused on one event.

While most previous studies paid attention to aerosol-induced changes in temperature, few studies examined the aerosol-caused changes in wind fields during heavily polluted haze events. Gao et al. (2016) found by using the WRF-Chem model that BC absorption led to anomalous northeasterlies in the eastern NCP due to its direct and semi-direct radiative effects during a heavily polluted event of 16–19 January 2010. Qiu et al. (2017) used the WRF-Chem model and found that, in a heavily polluted episode occurred in NCP in February 2014, the DRE of absorbing aerosols caused strong anomalous northeasterlies but that of scattering aerosols had a weak effect on winds. Li et al. (2020) used the Regional Integrated Evironmental Model System coupled with chemistry (RIEMS-Chem) to investigate a heavily polluted event in NCP during 20–26 February 2014, and also found ADE led to a strong anomalous northerlies in the eastern NCP during the episode.

This study aims to quantify the effects of aerosol DRE on meteorological variables during severe haze events by composite analyses on model results of the WRF-Chem model. The purpose of composite analysis is to find

Table 1

Summary of Previous Observational Studies That Reported Aerosol Radiative Effect in North China Plain During Severe Haze Events

Obversational study

Site	Time	Change in radiative flux at the surface (W m^{-2})		PM$_{2.5}$ concentration at the surface (µg m^{-3})		Reference
		Mean	Maxi.	Mean	Maxi.	
Beijing-CAMS[a] (39.93°N, 116.32°E)	1–31 January 2013	−26 ± 13			405	Bi et al. (2014)
Beijing-IAP[b] (39.98°N, 116.38°E)		−27 ± 13				
Beijing-RADI[c] (40.00°N, 116.38°E)		−27 ± 15				
Beijing-CAMS[a] (39.93°N, 116.32°E)	10–16 January 2013	−200			520	Che et al. (2014)
Beijing-RADI[c] (40.00°N, 116.38°E)						
Beijing-Nanjiao (39.80°N, 116.47°E)						
Beijing-IAP[b] (39.98°N, 116.38°E)	1–31 January 2013		−163		590	Yu et al. (2016)
Beijing-CAMS[a] (39.93°N, 116.32°E)	15–22 December 2016		−227		416	Zheng, Che, Xia, et al. (2017)
Shijiazhuang-SMB[d] (38.04°N, 114.42°E)			−199		676	
Jiaozuo-HPU[e] (35.19°N, 113.28°E)			−199		677	
Beijing-CAMS[a] (39.93°N, 116.32°E)	8–12 December 2016		−130		193	Zheng, Che, Yang, et al. (2017)
Beijing-Xianghe (39.75°N, 116.96°E)			−150			
Beijing-Shangdianzi (40.65°N, 117.12°E)			−110			
Baoding-Gucheng (39.13°N, 115.67°E)	1 December 2016–31 January 2017	−90			737	Liu et al. (2019)

[a]CAMS, Chinese Academy of Meteorological Sciences. [b]IAP, Institute of Atmospheric Physics. [c]RADI, Institute of Remote Sensing and Digital Earth, Chinese Academy of Sciences. [d]SMB, Shijiahzhuang Meteorological Bureau. [e]HPU, Henan Polytechnic University.

Table 2
Summary of Modeling Studies That Reported the Impacts of ARE on Meteorology During Severe Haze Events

Modeling study

Region	Time	Change in radiative flux at the surface (W m^{-2})		Change in temperature at the surface (°C)		PM$_{2.5}$ concentration at the surface (μg m^{-3})		ARE	Reference
		Mean	Maxi.	Mean	Maxi.	Mean	Maxi.		
BTH (36.2–41.0°N, 114.0–118.0°E)	10–15 January 2013	−20 to −140		−0.8 to −2.8		138 (in Beijing)	600	DRE[a] + IRE[b]	Gao et al. (2015)
NCP (36.2–41.0°N, 114.0–118.0°E)	11–24 January 2010		−440		−7	122 (in Beijing)	350	DRE[a] + SDE[c]	Gao et al. (2016)
NCP (37.9–42.4°N, 113.9–119.6°E)	21–27 February 2014	−55		−1.7		171	395	DRE[a]	Qiu et al. (2017)
NCP	15–21 December 2016	−80		−0.85		329		DRE[a]	Liu et al. (2019)
BTH (Beijing, Tianjin and Hebei)	1–31 January 2014	−50		−1.3		104		DRE[a] + SDE[c]	Zhang et al. (2018)
BTH (31.2–42.5°N, 113.3–122.6°E)	5 December 2015–4 January 2016		−180		−3.2		395	DRE[a] + IRE[b]	Wu et al. (2019)
BTH (Beijing, Tianjin and Hebei)	17–19 January 2010	−12		−0.7		230		DRE[a]	Gao et al. (2020)
BTH (Beijing, Tianjin and Hebei)	20–26 February 2014	−57		−1.8		116		DRE[a]	Li et al. (2020)
BTH (35.0–43.0°N, 113.0–121.1°E)	1–31 December 2015	−28 to 0		−0.3 to −0.5			465	DRE[a]	Wen et al. (2020)

Note. ARE, aerosol radiative effect; BTH, Beijing-Tianjin-Hebei; NCP, North China Plain.
[a]DRE, Mean aerosol direct radiative effect. [b]IRE, Aerosol indirect radiative effect. [c]SDE, Aerosol semi-direct radiative effect.

the common characteristics among episodes. Five heavily polluted events (15–17 January 2014, 13–15 January 2015, 8–10 December 2015, 21–23 December 2015, and 29–31 December 2016) in NCP were selected, in which episodes of 15–17 January 2014, 13–15 January 2015, and 21–23 December 2015 belong to the most dominant weather pattern for SPPDs and the rest of the episodes belong to the second most dominant weather pattern for SPPDs, as classified by Li et al. (2019). The most dominant weather pattern for SPPDs has a strong cold high at the surface, and the maximum pressure is over Mongolia. NCP is located within the southern region of this high in this case. The second most dominant weather pattern for SPPDs has a weak cold high at the surface that covers from Xinjiang autonomous region to the entire middle China, and hence the whole eastern China has uniform pressure (a small pressure gradient), leading to weak winds that are conducive to the formation of SPPDs. These two weather patterns were associated with 35.7% and 31.2% of the observed SPPDs in NCP, respectively (Li
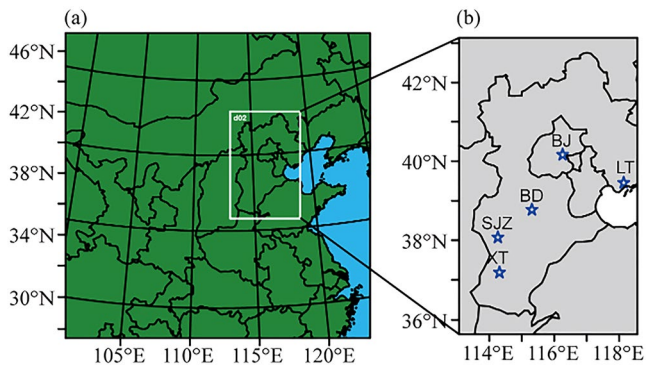
Figure 1. Model domains. (a) The outer domain (d01) has a horizontal resolution of 30 km. The white square indicates the inner domain (d02). (b) The inner domain North China Plain region (35.5°–42.5°N, 113.4°–119.8°E) has a resolution of 10 km. Beijing (BJ), Baoding (BD), Shijiazhuang (SJZ), Xingtai (XT), and Laoting (LT) are marked in the figure.

et al., 2019). This work is structured as follows. Section 2 describes the configuration of the WRF-Chem model, emission inventories, numerical experiments, and the observational data used in this work. Section 3 is the evaluation of simulated meteorological and chemical variables. Section 4 shows simulated $PM_{2.5}$ concentrations and aerosol DRE. Section 5 shows the simulated changes in meteorological fields by aerosol DRE. Section 6 sumarizes the conclusions of this work.

2. Model Description and Observation Data

2.1. Configuration of WRF-Chem Model

The WRF-Chem model (version 3.6) is an online-coupled model of chemistry and meteorology developed by National Center for Atmospheric Research (NCAR) and National Centers for Environmental Prediction. The WRF-Chem model used in this study is set with two nested domains. The horizontal resolution of the outer domain (d01) is 30 km and of the inner domain (d02) is 10 km. Vertically, the atmosphere from the ground to 50 hPa is divided into 30 layers. The number of horizontal grids is 75×75 for d01 and 52×79 for d02. The outer domain of the model covers most areas of China, and the inner domain (NCP, 35.5°–42.5°N, 113.4°–119.8°E) mainly covers Beijing, Tianjin, Hebei province, and a fraction of Shandong province (Figure 1).

The major physical schemes of the WRF-Chem model used in this work include the Lin microphysics scheme that accounts for the roles of aerosols in CCN and IN (Chen & Sun, 2002; Lin et al., 1983), the Rapid Radiative Transfer Model for GCMs (RRTMG) for short-wave and long-wave radiation (Zhao et al., 2010), the Yonsei University (YSU) scheme for planetary boundary layer (Hong et al., 2006), the Noah Land Surface Model scheme (Chen & Dudhia, 2001), and the Grell-Freita cumulus scheme (Grell & Freitas, 2014). With respect to the chemical schemes, the Fast-J scheme calculates photolysis rates (Wild et al., 2000) and the CBMZ (Carbon Bond Mechanism version Z) simulated the photochemical mechanism. The MOSAIC (Model for Simulating Aerosol Interactions and Chemistry) aerosol model (Zaveri & Peters, 1999; Zaveri et al., 2008) divides aerosols into eight size bins of 0.039–0.078, 0.078–0.156, 0.156–0.3125, 0.3125–0.525, 0.525–1.25, 1.25–2.5, 2.5–5.0, and 5.0–10 μm. The aerosol species in the MOSAIC scheme include sulfate (SO_4^{2-}), nitrate (NO_3^-), ammonium (NH_4^+), black carbon (BC), organic carbon (OC), sodium (Na^+), chloride (Cl^-), liquid water, but secondary organic aerosol (SOA) was not included. Aerosols are assumed to be internally mixed in each size bin and externally mixed among eight size bins. Detailed physical and chemical configurations are listed in Table 3. Initial and boundary conditions of meteorology were taken from the NECP Final Analysis (FNL) data with a horizontal resolution of $1° \times 1°$ for every 6 hr. Chemical initial and boundary conditions were from MOZART-4 (Model for Ozone and Related chemical Tracers) forecasts (Emmons et al., 2010).

2.2. Emission

The Multi-resolution Emission Inventory of China for years of 2014, 2015, and 2016 (http://www.meicmodel.org/) were used in the model for anthropogenic emissions. The spatial resolution of these emissions is $0.25° \times 0.25°$. This monthly anthropogenic inventory includes 10 major atmospheric chemical components, such as sulfur dioxide (SO_2), nitrogen oxides (NO_x), carbon monoxide (CO), ammonia (NH_3), non-methane volatile organic compounds (NMVOCs), primary PM_{10}, primary $PM_{2.5}$, BC, OC, and carbon dioxide (CO_2) from five sectors of power, industry, residential, transportation and agriculture. We used the Model of Emissions of Gas and Aerosols from Nature (MEGAN) (Guenther et al., 2006) to calculate biogenic emissions. Biomass burning emissions were obtained from the Fire Inventory from NCAR (FINN) data set (Wiedinmyer et al., 2011). For each simulation, we spun up the model for 64 hr and then integrated over each event. We used the local time in this paper.

2.3. Numerical Experiments

We carried out simulations for five severe pollution events (Type1_1, 15–17 January 2014; Type1_2, 13–15 January 2015; Type1_3, 21–23 December 2015; Type2_1, 8–10 December 2015; Type2_2, 29–31 December

Table 3
The Weather Research and Forecasting-Chemistry Physical and Chemical Schemes for This Study

Scheme	Description
Microphysics scheme	Lin microphysics scheme[a]
Short-wave and Long-wave radiation schemes	RRTMG[b]
Planetary boundary layer scheme	Yonsei University Scheme (YSU)[c]
Land surface scheme	Noah Land Surface Model scheme[d]
Cumulus parameterization scheme	Grell-Freita cumulus scheme[e]
Photolysis rates scheme	Fast-J[f]
Gas-phase chemistry scheme	CBMZ mechanism[g]
Aerosol module	MOSAIC[h]

Note. CBMZ, Carbon Bond Mechanism version Z; MOSAIC, Model for Simulating Aerosol Interactions and Chemistry; RRTMG, Rapid Radiative Transfer Model for GCMs.
[a]Lin et al. (1983). [b]Zhao et al. (2010). [c]Hong et al. (2006). [d]Chen and Dudhia (2001). [e]Grell and Freitas (2014). [f]Wild et al. (2000). [g]Zaveri and Peters (1999). [h]Zaveri et al. (2008).

2016), all of which lasted for four days or longer. Type 1 and Type 2 are the first and second most dominant weather patterns identified for SPPDs in NCP (Li et al., 2019). For each of the five events, we carried out two simulations named "CTRL" and "NODIR." The CTRL experiment simulates interactive meteorological fields and chemistry/aerosols, taking into consideration of aerosol direct and indirect radiative effects. The NODIR experiment is the same as CTRL, but DRE of all aerosols was turned off. The removal of aerosol DRE is achieved by setting the mass of all aerosol species to be zero in the simulation of aerosol optical properties. The differences between CTRL and NODIR simulation (CTRL—NODIR) for each case quantify the impacts of aerosol DRE on meteorology.

2.4. Observation Data

In order to evaluate the accuracy of the model, we used meteorological and chemical observations. The observed meteorological variables at the surface include 3-hourly time series of 2-m temperature (T2), 2-m relative humidity (RH2), 10-m wind speed (WS10), and 10-m wind direction (WD10) from NOAA's National Climatic Data Center (http://gis.ncdc.noaa.gov/maps/ncei/cdo/hourly). We used meteorological measurements from 26 stations in the NCP region (Table S1 in Supporting Information S1). The daily surface total radiation for Beijing (39.48°N, 116.28°E) and Laoting (39.26°N, 118.53°E) were obtained from China Meteorological Data Service Center (http://data.cma.cn). These two stations had observed surface total radiation for the time periods we studied. Hourly PM$_{2.5}$ data were used to evaluate whether the model can capture well the concentrations of pollutants during the five haze events in NCP, which were collected from the China National Environmental Monitoring Center (CNEMC) (http://www.cnemc.cn). We used observations at 125 stations in the NCP region in this study, which were located in 22 cities shown in Table S2 in Supporting Information S1. For each city, the concentrations of PM$_{2.5}$ were averaged over all the stations within this city. After eliminating the missing values, more than 90% of data are valid in each city.

3. Simulated PM$_{2.5}$ and Meteorology in the Five Haze Events and Model Evaluation

3.1. Concentrations of PM$_{2.5}$

Figure 2 shows, for each case, the simulated spatial distribution of PM$_{2.5}$ in NCP from the CTRL run that is averaged over the pollution event. Simulated PM$_{2.5}$ concentrations exceeded 150 μg m^{-3} in all the cases, with the highest maximum of 372 μg m^{-3} in the case of Type2_1 and the lowest maximum of 190 μg m^{-3} in the case of Type2_2. The area with PM$_{2.5}$ > 150 μg m^{-3} covered a large fraction of Hebei province in cases of Type1_1, Type1_3, and Type2_1, while it covered relatively small fraction of the province in the rest cases.

Figure 2 also shows, for each case, the time variations of observed and simulated hourly concentrations of PM$_{2.5}$ averaged over the 22 cities. The model did well with the simulation of the temporal variations of PM$_{2.5}$. The
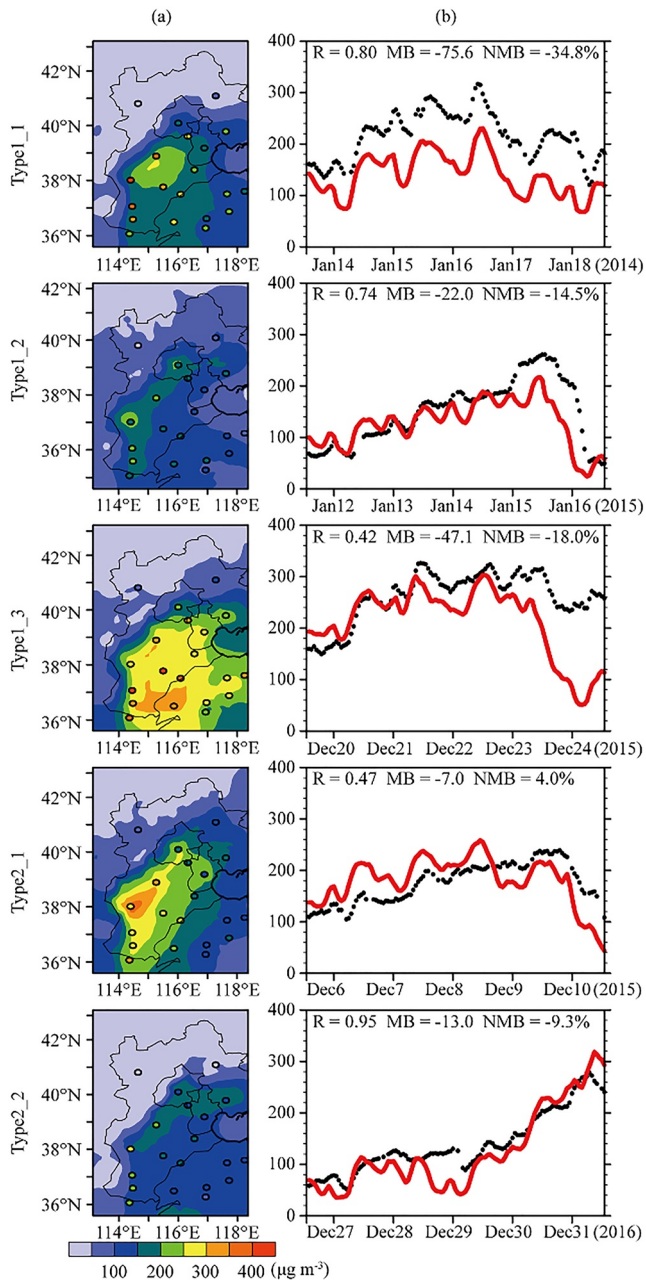
Figure 2. (a) Simulated PM$_{2.5}$ concentrations (µg m^{-3}) in North China Plain (NCP) that were averaged over each event (a–e). The circles are the observed concentrations at 22 cities. (b) Time series of observed (black dots) and simulated (red lines) hourly PM$_{2.5}$ concentrations (µg m^{-3}) averaged over the 22 cities in NCP for the five cases. The simulated values were from the corresponding grid points of 22 cities. The mean bias (MB), normalized mean bias (NMB) and correlation coefficient (R) are indicated in panels of Figure 2b. $MB = \frac{1}{n} \times \sum_{i=1}^{n} (SIM_i - OBS_i)$, $NMB = \frac{\sum_{i=1}^{n} (SIM_i - OBS_i)}{\sum_{i=1}^{n} OBS_i} \times 100\%$, in which OBS$_i$ and SIM$_i$ represent the hourly observed and simulated data, respectively, and n denotes the total number of hours.

correlation coefficients between modeled and observed hourly concentrations were 0.80, 0.74, 0.47, 0.42, 0.95, respectively, in the five cases. The model captured fairly well the magnitudes of PM$_{2.5}$ concentrations. Compared with measurements, the modeled concentrations of PM$_{2.5}$ in the five cases had mean biases (MB) and the normalized mean biases (NMB, in brackets) of −75.6 µg m^{-3} (−34.8%), −22.0 µg m^{-3} (−14.5%), −47.1 µg m^{-3} (−18.0%), 7.0 µg m^{-3} (4.0%), −13.0 µg m^{-3} (−9.3%), respectively. The model underestimates PM$_{2.5}$ concentrations in all cases except Type2_1. The underestimation of PM$_{2.5}$ was also reported in previous simulations of severe haze events using WRF-Chem. The possible reasons are the biases in simulated meteorology, the uncertainties in emissions, and the lack of some atmospheric chemical pathways. As shown below in Section 3.2, the model underestimates RH2 and overestimates WS10, which would underestimate the water uptake by aerosols and overestimate the horizontal dispersion of pollutants, respectively. In addition, the WRF-Chem model does not include anthropogenic emissions of dust (Xia et al., 2022), and it has biases in simulating the formation of sulfate in clouds (Sha et al., 2022). All of these processes could contribute to the underestimation of PM$_{2.5}$ concentrations in this work.

3.2. Meteorological Parameters

For meteorological parameters, we used 3-hourly data to compare the simulated and observed values. The averaged T2 of each of the 5 haze events ranged from 269.4 to 274.1 K in NCP. The model reproduced well the 3-hourly variations in T2 in NCP in the five cases (Figure 3), with high correlation coefficients (0.89–0.96) between simulated and observed T2. The MBs and NMBs were, respectively, 1.1 K (0.2%), 1.9 K (0.7%), 0.9 K (0.3%), 1.0 K (0.4%), 1.6 K (0.6%) in the five cases. During the haze events, relative humidity was general high, with RH2 values in the range of 43.4%–72.6% during daytime and of 51.9%–79.7% during nighttime. In the five cases, for RH2, the correlation coefficients between observations and model results were 0.79, 0.94, 0.79, 0.91, 0.88, and the MBs and NMBs were −7.8% (−14.2%), −0.7% (−1.2%), −12.3% (−17.1%), 0.6% (0.8%), −7.9% (−12.8%), respectively. The negative biases in RH2 could contribute to the underestimation of PM$_{2.5}$ shown in Figure 2b because of the weakened hygroscopic growth of aerosols (Wang et al., 2013).

Daily wind speeds during the haze events were generally low and the mean values were lower than 3.5 m s^{-1}. In the five cases, the correlation coefficients between the modeled and observed 3-hourly WS10 were 0.64, 0.91, 0.24, 0.87, 0.70, respectively, and MBs and NMBs were 0.9 m s^{-1} (40.7%), 1.15 m s^{-1} (52.9%), 0.9 m s^{-1} (52.0%), 1.1 m s^{-1} (57.6%), 1.2 m s^{-1} (52.3%), respectively. The high biases in wind speed were a common issue in previous studies that used the WRF-Chem model (Zhang et al., 2018; Gao et al., 2015; Qiu et al., 2017). The overestimation of WS10 could lead to the underestimation of PM$_{2.5}$ shown in Figure 2b, which is favorable for the dispersion of pollutants (Cai et al., 2017).

Wind directions were evaluated at four sites in NCP with high PM$_{2.5}$ levels, including Beijing, Baoding, Shijiazhuang, and Xingtai from the north to the south of NCP (marked in Figure 1). Figure 4 shows the variations in observed and simulated 10-m wind direction (WD10) at these locations for the five studied cases. Because the wind direction is a vector, it is unreliable to use the correlation coefficient to evaluate the consistency between the model results and the observations. Therefore the index of agreement (IOA) was used to evaluate the simulated wind direction (see the caption of Figure 4
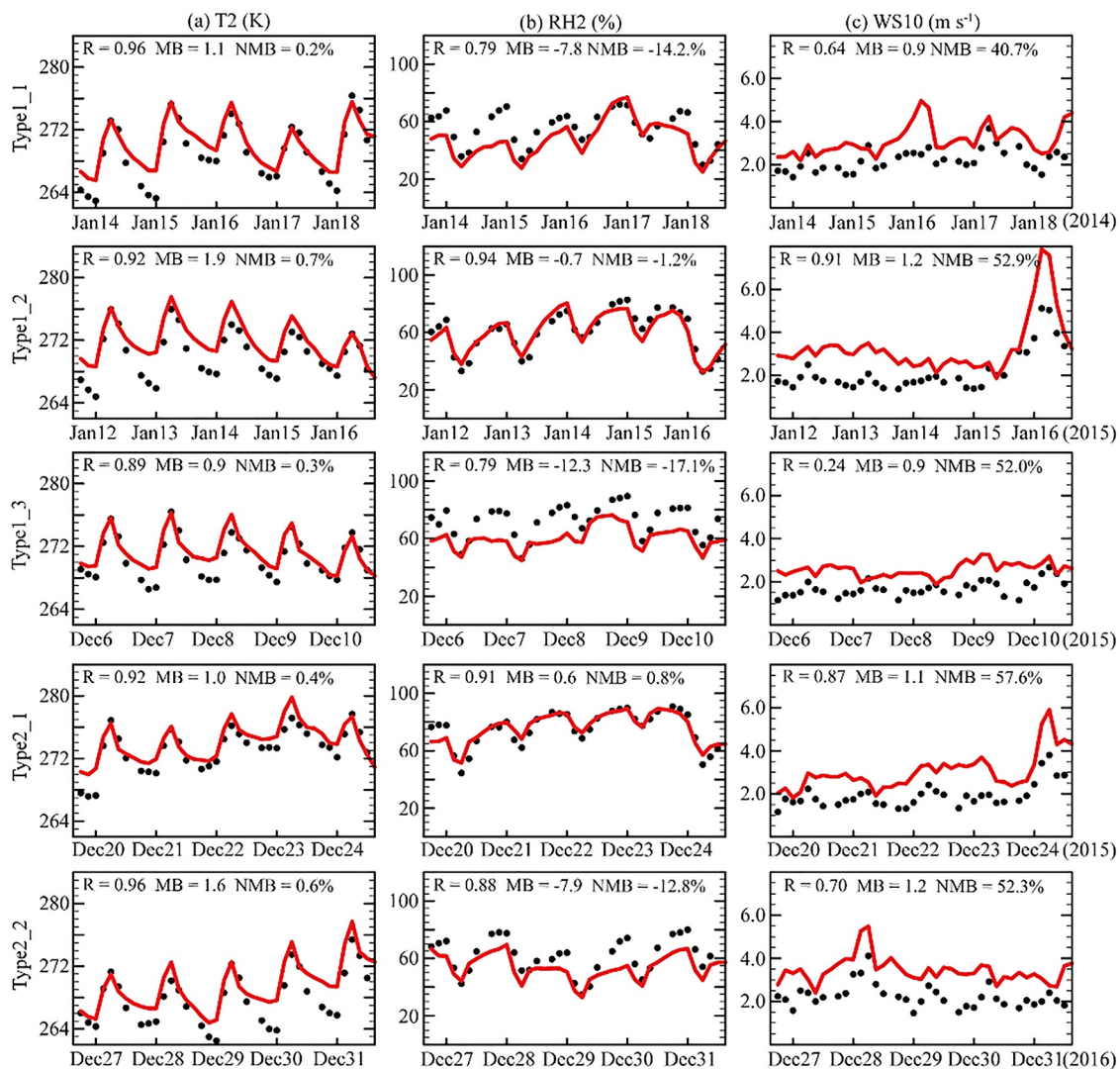
Figure 3. Time series of (a) 2-m temperature (T2, °C), (b) 2-m relative humidity (RH2, %), (c) 10-m wind speed (WS10, m s^{-1}) for the five cases from observations (black dots) and model results (red lines). Observed T2 in each case was the average of the observations at 26 stations in North China Plain. The simulated values were from the corresponding grid points of the 26 stations.

for the formula of calculation). The value of 1 indicates an exact match, and 0 indicates no consistency (Chen et al., 2019). IOA values were in the range of 0.42–0.81 (Figure 4), indicating that the model can capture wind direction fairly well. The uncertainties in wind fields were reported to be caused by the default setup in surface land cover in WRF-Chem (Wang et al., 2012).

Figure 5 compares for the five cases the simulated and observed daily mean total radiation (shortwave plus longwave) at the surface at the stations in Beijing (BJ) and Laoting (LT) (marked in Figure 1) where observations are available. Positive values indicate downward radiation. The correlation coefficients, MBs, and NMBs between the simulated and observed daily total radiation were summarized in Table 4. The model can simulate the variations in daily total radiation in the five cases fairly well with correlation coefficients of 0.68, 0.85, 0.47, 0.92, 0.88 in Beijing and of 0.97, 0.70, 0.63, 0.60, 0.95 in Laoting. The MBs (NMBs) in the five cases were 0.1 W m^{-2} (0.1%), 16.4 W m^{-2} (24.4%), 12.0 W m^{-2} (22.3%), −5.7 W m^{-2} (−10.2%), −13.9 W m^{-2} (−15.7%) in Beijing and 19.3 W m^{-2} (24.8%), 31.8 W m^{-2} (48.1%), 12.0 W m^{-2} (20.1%), 12.7 W m^{-2} (20.4%), −5.5 W m^{-2} (−6.6%) in Laoting, respectively. It should be noted that the simulated downward shortwave fluxes were larger than the net downward total radiative fluxes because of the opposite directions of shortwave and longwave radiative fluxes at the surface. The simulated variations in shortwave radiation dominated the variations in total radiation.
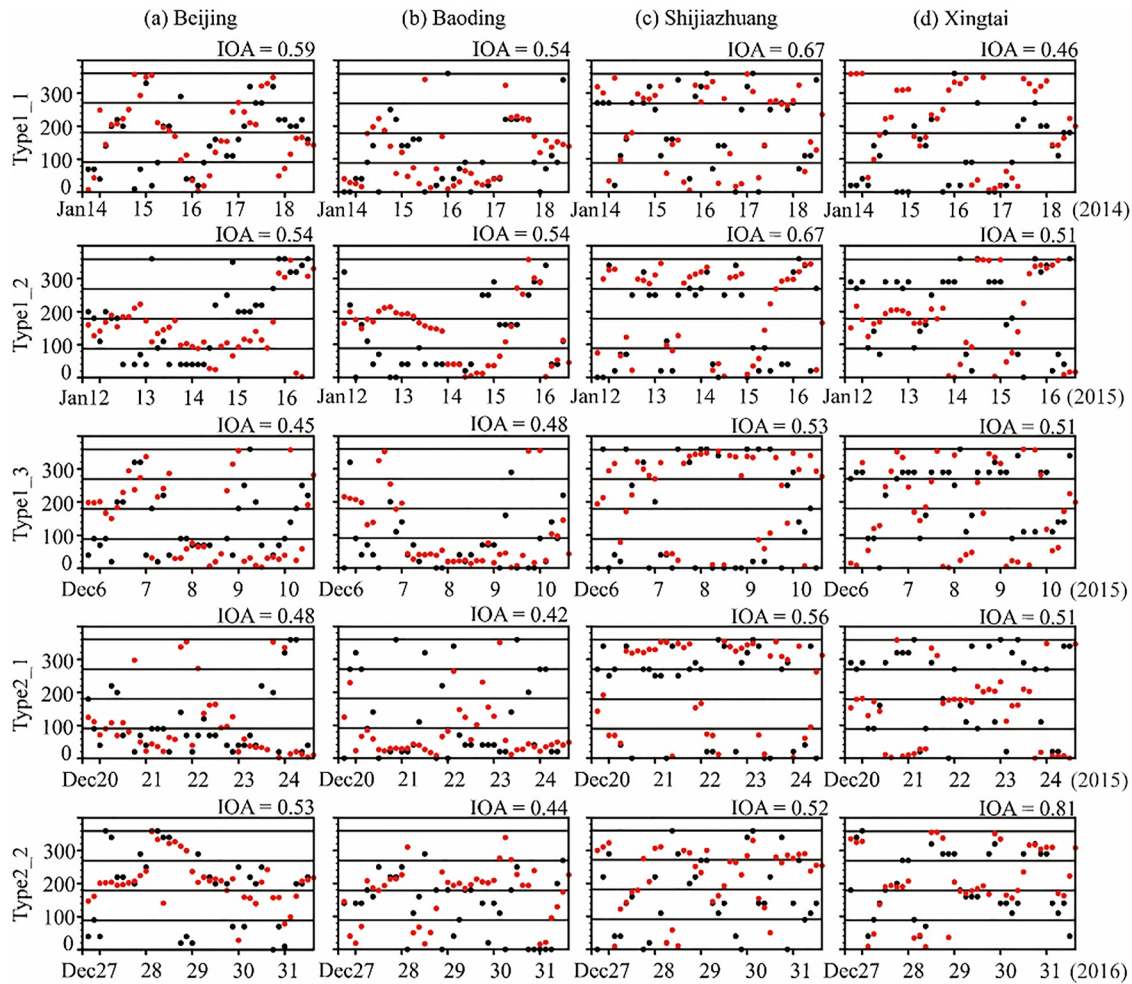
Figure 4. Time series of 10-m wind direction (degree) in (a) Beijing, (b) Baoding, (c) Shijiazhuang, (d) Xingtai for the five cases from observations (black dots) and model results (red dots). The simulated values were from the corresponding grid points of these 4 cities. 0 or 360, 90, 180, 270° represent winds from the north, east, south, and west, respectively. Index of agreement (IOA) is the index of agreement between observed and simulated 10-m wind directions.

$$IOA = 1 - \frac{\sum_{i=1}^{n}\left(SIM_i - OBS_i\right)^2}{\sum_{i=1}^{n}\left(|OBS_i - \overline{OBS}| + |SIM_i - \overline{SIM}|\right)^2},$$ where OBS_i and SIM_i represent the observed and simulated hourly data, respectively, n denotes the total number of hours, and $\overline{OBS}$ and $\overline{SIM}$ represent the averages of observations and model results, respectively.

4. Simulated PM$_{2.5}$ Concentrations and Aerosol DRE

4.1. PM$_{2.5}$ Concentrations

Figures 6a and 6b show, respectively, the horizontal and vertical distributions of PM$_{2.5}$ concentrations from the CTRL simulation averaged over each event. The red lines in Figure 6a indicate the areas with PM$_{2.5}$ values > 150 µg m^{-3}. The total area with PM$_{2.5}$ > 150 µg m^{-3} was the largest in Type1_3 and the smallest in Type1_2. Averaged over the areas with PM$_{2.5}$ > 150 µg m^{-3} and over the event, the PM$_{2.5}$ concentrations reached 197.3, 187.0, 291.9, 215.8, 178.1 µg m^{-3} in the five cases, respectively. Vertically, aerosol concentrations generally decreased with altitude. It should be noted that the Taihang mountain exists in the west of NCP. The PM$_{2.5}$ concentrations at the surface were the highest (reached about 205.7, 248.5, 527.6, 376.2, 149.8 µg m^{-3} in the five cases, respectively) and became very small above 700 hPa (less than 5 µg m^{-3}) (Figure 6b).

4.2. Net Shortwave Radiative Flux at the Surface

Figure 7a shows the net shortwave flux at the surface (SRFs) from the CTRL simulation averaged over each event. The net SRFs were relatively lower in the areas with PM$_{2.5}$ > 150 µg m^{-3} because of the DRE by aerosols.
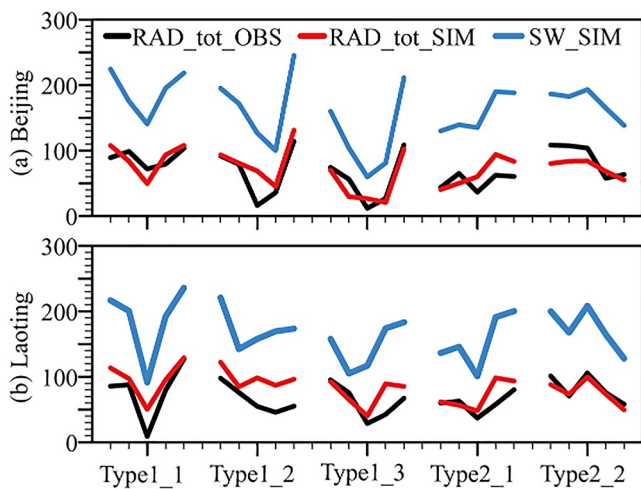
Figure 5. Observed (black lines) and modeled (red lines) daily mean total radiative flux (W m^{-2}, shortwave plus longwave) as well as the simulated daily mean shortwave radiative flux (blue lines) (W m^{-2}) at the surface in (a) Beijng and (b) Laoting, for the five cases.

Averaged over the areas with PM$_{2.5}$ > 150 μg m^{-3}, the values of SRFs were 231.1, 215.1, 190.6, 193.6, and 252.0 W m^{-2} in the five cases, respectively.

Figure 7b shows the changes in net shortwave radiative flux at the surface (ΔSRFs) caused by aerosol DRE (CTRL minus NODIR) averaged over each event. The averaged ΔSRFs over the areas with PM$_{2.5}$ > 150 μg m^{-3} and over the event were −86.7, −70.0, −85.8, −68.1, and −52.1 W m^{-2} in the five cases, respectively. The averaged ΔSRFs over the NCP and over the event were −47.1, −48.7, −51.5, −37.6, and −29.3 W m^{-2} in the five cases, respectively, which agreed closely with the value of −55 W m^{-2} reported for NCP in Qiu et al. (2017) and −57 W m^{-2} reported for BTH in Li et al. (2020) (Table 2).

Comparing Figure 7b with Figure 6a, we found that the changes in shortwave radiative fluxes at the surface basically corresponded to the distributions of PM$_{2.5}$ concentrations. The higher the PM$_{2.5}$ concentrations, the larger the reductions in SRFs. In Type1_3, the absolute changes in SRFs were the highest, corresponding to the highest PM$_{2.5}$ concentrations among five cases (291.9 μg m^{-3} averaged over the areas with PM$_{2.5}$ > 150 μg m^{-3} and over the event.). In Type2_2, the absolute changes in SRFs were the lowest, corresponding to the lowest PM$_{2.5}$ concentrations in five cases (178.1 μg m^{-3} averaged over the areas with PM$_{2.5}$ > 150 μg m^{-3} and over the event.) (Figure 6a). We used the values of ΔSRFs/PM$_{2.5}$ and ΔSRFs/column burden of PM$_{2.5}$ to show the sensitivity of ΔSRFs to PM$_{2.5}$ levels, aiming to obtain the range of sensitivities considering that ΔSRFs can be influenced by factors such as the vertical profile of aerosols, the chemical components of aerosols, relative humidity, the presence of clouds, or weather patterns. For the five cases, the values of ΔSRFs/PM$_{2.5}$ averaged over the areas with PM$_{2.5}$ > 150 μg m^{-3} (calculated first the ratio of each grid in NCP, and then averaged over the areas with PM$_{2.5}$ > 150 μg m^{-3}) were −0.46, −0.40, −0.31, −0.34, −0.31 W m μg^{-1}, respectively (Figure 10a). We also calculated the values of ΔSRFs/column burden of PM$_{2.5}$ (Figure S3a in Supporting Information S1). For the five cases, the values of ΔSRFs/column burden of PM$_{2.5}$ averaged over the aeras with PM$_{2.5}$ > 150 μg m^{-3} were −6.08, −4.93, −4.75, −4.38, −5.75 10^{-4} W μg^{-1}, respectively. Our results suggest that ΔSRFs/PM$_{2.5}$ are related to aerosol optical properties other than weather patterns, since the values for the two types of weather pattern are very close.

5. Simulated Changes in Meteorological Fields by Aerosol DRE

5.1. Simulated Changes in Temperature

Figures 8a and 8c show, respectively, the horizontal distributions of temperature at 2 m (T2) and vertical distributions of temperature from the CTRL simulation averaged over each event. Values of T2 were respectively, −0.13, 1.17, 1.97, 3.59, and −0.89°C in these five cases average over the area with PM$_{2.5}$ > 150 μg m^{-3}, so Type2_1 was the warmest event and Type2_2 was the coldest case. Vertically, temperature generally decreased with altitude.

Figures 8b and 8d show, respectively, the horizontal distributions of the changes in temperature at 2 m (ΔT2) and vertical distributions of the changes in temperature caused by aerosol DRE (CTRL minus NODIR) averaged over each event. Values of ΔT2 were, respectively, −0.63, −0.67, −0.81, −0.97, and −0.28°C in these five cases when averaged over the areas with PM$_{2.5}$ > 150 μg m^{-3}. Vertically, temperatures were reduced at the surface and increased around 850 hPa in all the five cases. Similar phenomenon was also reported in previous simulations of severe haze events using the WRF-Chem model (Gao et al., 2015, 2016). The cooling at the surface was caused by both the scattering aerosols (sulfate, nitrate, ammonium, and organic carbon) and absorbing aerosols (black carbon and week absorption of organic carbon) which reduced shortwave fluxes at the surface, and the warming around

Table 4
The Statistics Between the Simulated and Observed Daily Mean Total Radiative Fluxes at the Surface in Beijing and Laoting for the Five Cases

|		Type1_1	Type1_2	Type1_3	Type2_1	Type2_2
	R	0.68	0.85	0.47	0.92	0.88
BJ	MB	0.1	16.4	12.0	−5.7	−13.9
	NMB	0.1%	24.4%	22.3%	−10.2%	−15.7%
	R	0.97	0.70	0.63	0.60	0.95
LT	MB	19.3	31.8	12.0	12.7	−5.5
	NMB	24.8%	48.1%	20.1%	20.4%	−6.6%

*Note*. BJ, Beijing; LT, Laoting; MB, mean biases; NMB, normalized mean biases.
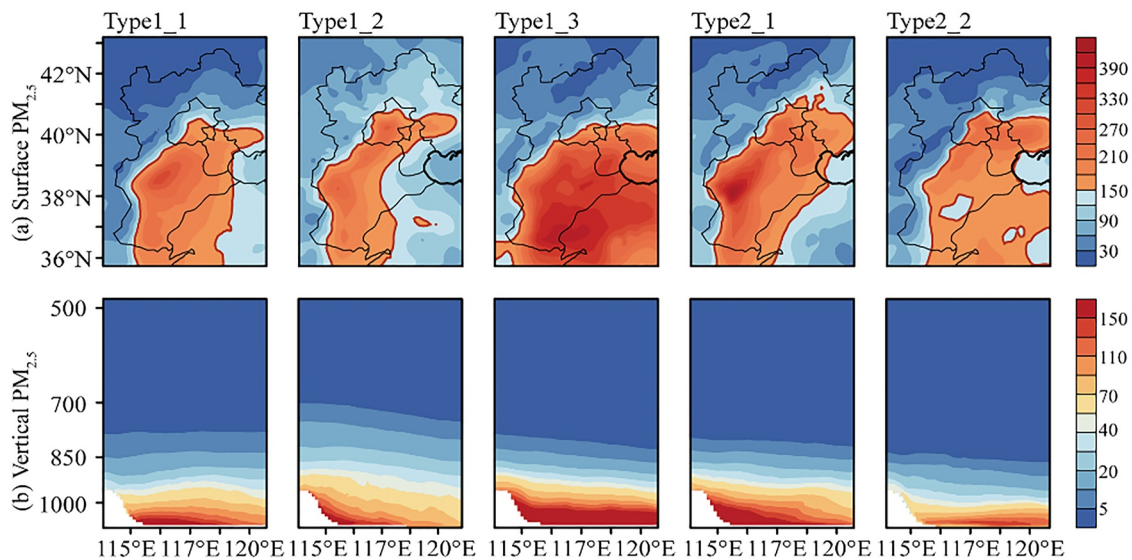
Figure 6. (a) Horizontal distributions of $PM_{2.5}$ concentrations (µg m^{-3}) in North China Plain from the CTRL simulation. The red lines indicate the areas with $PM_{2.5}$ concentration >150 µg m^{-3}. (b) Vertical distribution of $PM_{2.5}$ (µg m^{-3}) from the CTRL run. The cross sections were averaged over the latitudes of 35.5–42.5°N. All panels in (a and b) were averaged over each event.

850 hPa was caused by absorbing aerosols (Qiu et al., 2017). Chen et al. (2022), by using the WRF-Chem model, found that the different vertical profiles of BC always caused the largest warming in the lower troposphere instead of at the surface, because higher altitudes would have smaller BC concentration and lower altitudes would have weaker solar radiation for absorption. Wang et al. (2018) also reported that, although BC has its maximum concentration near the surface, the heating efficiency of BC due to the absorption of shortwave radiation peaked around 600–800 m. The maximum cooling was 1.03°C and the maximum warming at about 850 hPa was 0.59°C in Type1_3, corresponding to the highest $PM_{2.5}$ concentration in this case (Figure 6a).

It is of interest to estimate the changes in temperature per unit mass of $PM_{2.5}$. The distributions of $\Delta T2/PM_{2.5}$ were uneven (Figure 10b); large negative values of $\Delta T2/PM_{2.5}$ occurred within the regions with $PM_{2.5} > 150$ µg m^{-3}. For the five cases, the values of $\Delta T2/PM_{2.5}$ averaged over the region with $PM_{2.5} > 150$ µg m^{-3} were −0.33,
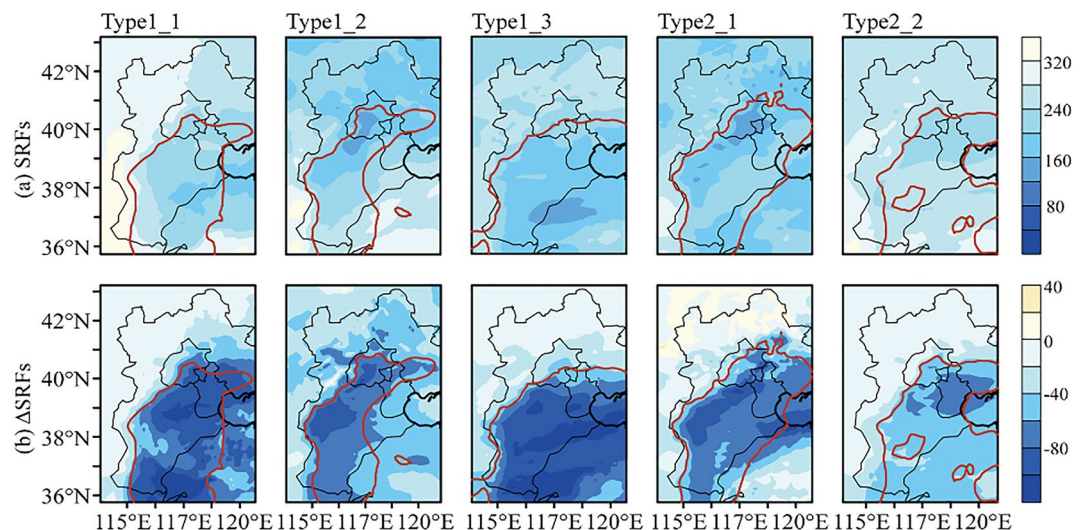
**Figure 7.** (a) Shortwave radiative flux at the surface (W m^{-2}) from the CTRL simulation that were averaged over each haze event. (b) The changes in shortwave radiative flux at the surface (W m^{-2}) caused by aerosol direct radiative effects (CTRL minus NODIR) averaged over each haze event. The red lines indicate the areas in North China Plain with $PM_{2.5}$ concentrations >150 µg m^{-3}.
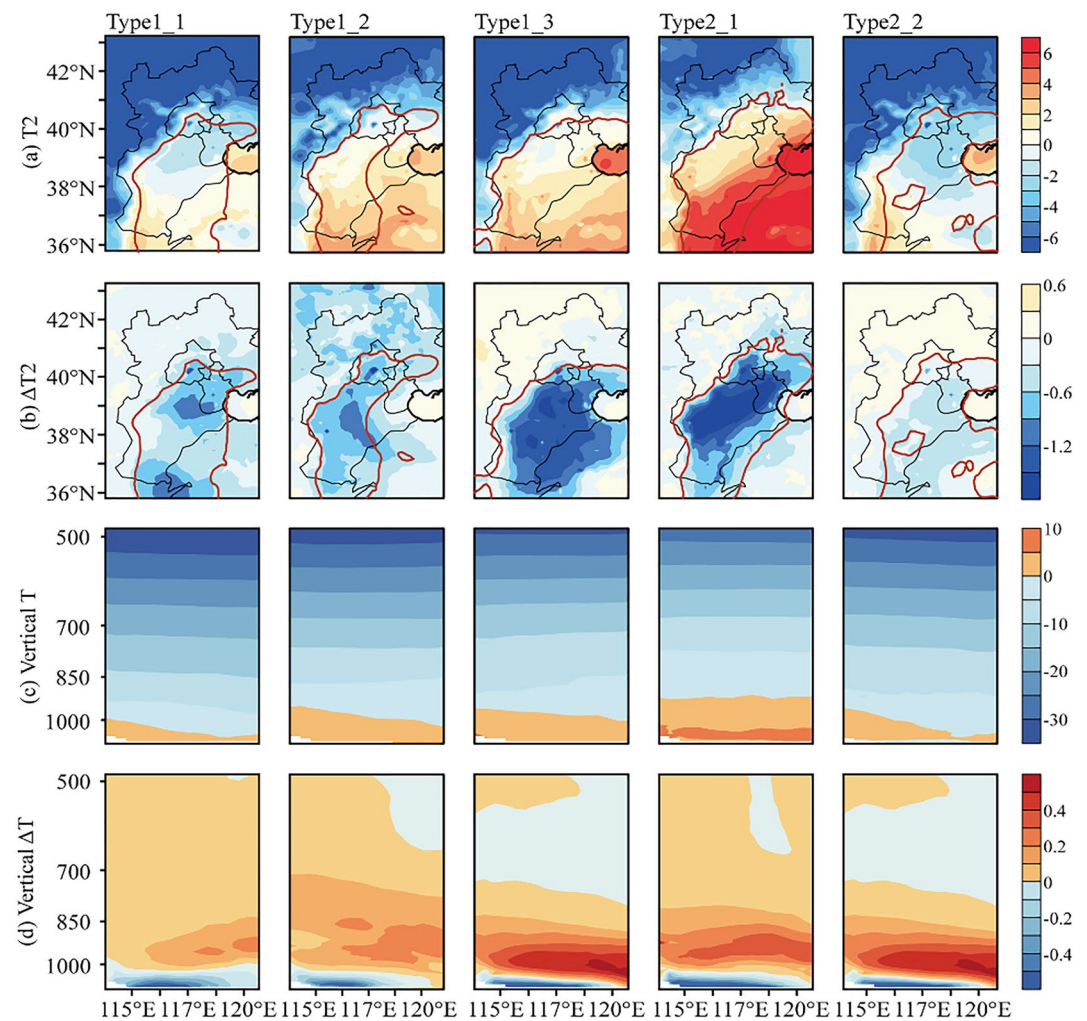
Figure 8. (a) Spatial distributions of 2-m temperature in North China Plain (NCP) (T2; °C) from the CTRL simulation. (b) Spatial distributions of the changes in T2 (°C) caused by aerosol direct radiative effects (DRE) (CTRL minus NODIR) (c) Vertical profiles of temperature (°C) in NCP from the CTRL simulation. (d) Vertical profiles of the changes in temperature (°C) caused by aerosol DRE (CTRL minus NODIR). All the panels in (a–d) were the averages over each event. The red lines in (a and b) indicate the areas in NCP with $PM_{2.5}$ concentrations >150 μg m^{-3}. The cross sections in (c and d) were averaged over the latitudes of 35.5–42.5°N.

−0.36, −0.26, −0.44, −0.16°C m^3 μg^{-1} 10^{-2}, respectively. It should be noted that $\Delta T2/PM_{2.5}$ was the largest (−0.44°C m^3 μg^{-1} 10^{-2}) in Type2_1 and the smallest (−0.16°C m^3 μg^{-1} 10^{-2}) in Type2_2. The changes in T2 caused by aerosol DRE can be influenced by winds (wind speed and wind direction) as well as the convergence/ divergence of winds. The averaged 10-m wind speeds over the regions with $PM_{2.5}$ > 150 μg m^{-3} were 0.93, 1.21, 1.13, 1.18, 2.33 m s^{-1} in the five cases (Figure S1a in Supporting Information S1), respectively. In Type2_2, the averaged wind speed was the highest (2.33 m s^{-1}), which diluted the cooling caused by aerosol DRE and contributed to the weakest cooling of $\Delta T2/PM_{2.5}$ of −0.16°C m^3 μg^{-1} 10^{-2}. Considering the 10-m divergence for the five cases (Figure S1b in Supporting Information S1), the averaged values of divergence over the aeras with $PM_{2.5}$ > 150 μg m^{-3} was −0.001, 0.007, −0.018, −0.023, and 0.089 10^{-5} s^{-1} in the five cases, respectively. Positive values in Type1_2 and Type2_2 indicate divergence and negative values in Type1_1, Type1_3 and Type2_1 indicate convergence. In Type2_1, the largest negative value of $\Delta T2/PM_{2.5}$ of −0.44°C m^3 μg^{-1} 10^{-2} was also associated with the largest convergence of −0.023 10^{-5} s^{-1}, which was not favorable to the transport of energy to the surrounding area and therefore temperature change was limited to the local area. On the contrary, the highest divergence (0.089 10^{-5} s^{-1}) in Type2_2 contributed to the weakest $\Delta T2/PM_{2.5}$ (−0.16°C m^3 μg^{-1} 10^{-2}). The surface cooling was also found to be associated with the intrusion of cold air mass. Figure S2 in Supporting
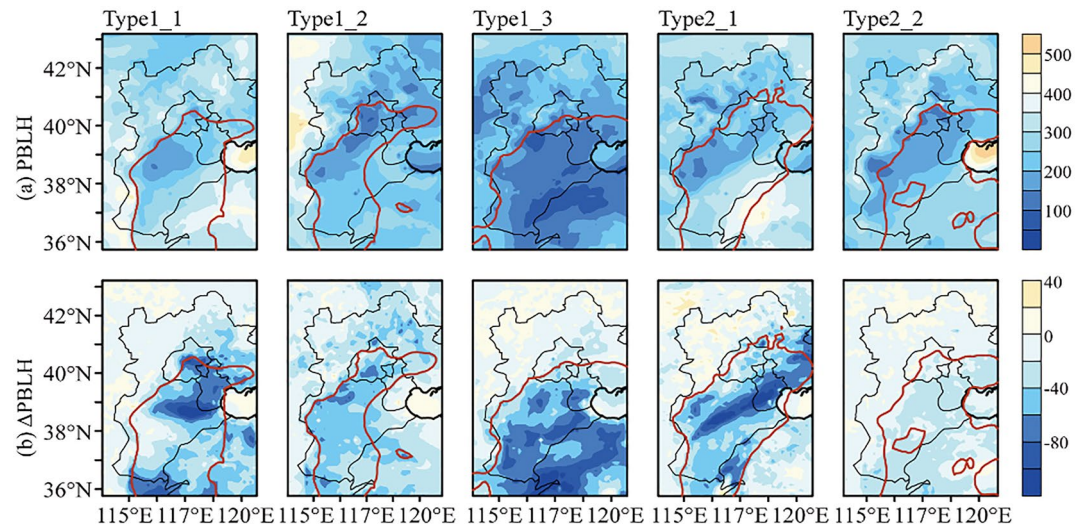
Figure 9. (a) Spatial distributions of planetary boundary layer height (PBLH; m) in North China Plain (NCP) from the CTRL simulation. (b) Spatial distributions of the changes in PBLH caused by aerosol direct radiative effects (CTRL minus NODIR). All the panels were the averages over each event. The red lines indicate the areas in NCP with $PM_{2.5}$ concentrations >150 µg m^{-3}.

Information S1 shows the daily variations in spatial distributions of $\Delta T2/PM_{2.5}$ and 10-m wind field for the five cases. Cases of Type1_1, Type1_2, Type1_3 and Type2_1 had strong northerlies or northwesterlies., Type2_1 had the most intense northerlies on the third day of the event, which can further explain the largest negative $\Delta T2/PM_{2.5}$ in this case. On the contrary, southerlies prevailed during the event of Type2_2, which contributed to the weakest cooling of $\Delta T2/PM_{2.5}$ of -0.16°C m^3 µg^{-1} 10^{-2}.

We also calculated the values of ΔT/column burden of $PM_{2.5}$ (Figure S3b in Supporting Information S1). For the five cases, the values of $\Delta T2$/column burden of $PM_{2.5}$ averaged over the aeras with $PM_{2.5} > 150$ µg m^{-3} were -4.42, -4.89, -4.06, -5.85, -3.11 10^{-6} °C m^2 µg^{-1}, respectively.

5.2. Simulated Changes in Planetary Boundary Layer Height

Figure 9a shows the spatial distributions of planetary boundary layer height (PBLH) from the CTRL simulation averaged over each event. The values of PBLH were generally lower in the areas with $PM_{2.5}$ concentrations >150 µg m^{-3} than the surrounding areas because of the positive feedback between $PM_{2.5}$ and PBLH (Qiu et al., 2017). Aerosols reduce the solar radiation reaching the ground, causing the decreases in surface temperature, which inhibit the development of the planetary boundary layer. Averaged over the areas with $PM_{2.5}$ concentrations >150 µg m^{-3}, the values of PBLH were 272.9, 201.8, 139.6, 263.7, and 234.8 m in the five cases, respectively. Type1_3 had the lowest PBLH, corresponding to the highest $PM_{2.5}$ concentrations in this case.

Figure 9b shows the spatial distributions of the changes in PBLH (ΔPBLH) caused by aerosol DRE (CTRL minus NODIR) that were averaged over each event. During the haze events, the averaged ΔPBLH values over the areas with $PM_{2.5}$ concentrations >150 µg m^{-3} were -49.7, -44.7, -58.5, -50.8, and -23.1 m in the five cases, respectively. Similar to ΔSRFs, ΔPBLH basically corresponded to the distributions of $PM_{2.5}$ concentrations. The higher the $PM_{2.5}$ concentrations the larger the reductions in PBLH. The heating effect in the upper PBL and the cooling effect of near the surface caused by aerosols increased the atmospheric stratification, leading to a substantial drop in PBLH (Ding et al., 2016). For the five cases, the values of ΔPBLH/$PM_{2.5}$ averaged over the region with $PM_{2.5} > 150$ µg m^{-3} were -0.25, -0.24, -0.20, -0.24, -0.13 m^4 µg^{-1}, respectively (Figure 10c). We also calculated the values of ΔPBLH/column burden of $PM_{2.5}$ (Figure S3c in Supporting Information S1). The values of ΔPBLH/column burden of $PM_{2.5}$ is -3.47, -3.18, -3.10, -3.25, -2.52 10^{-4} m^3 µg^{-1}, respectively.
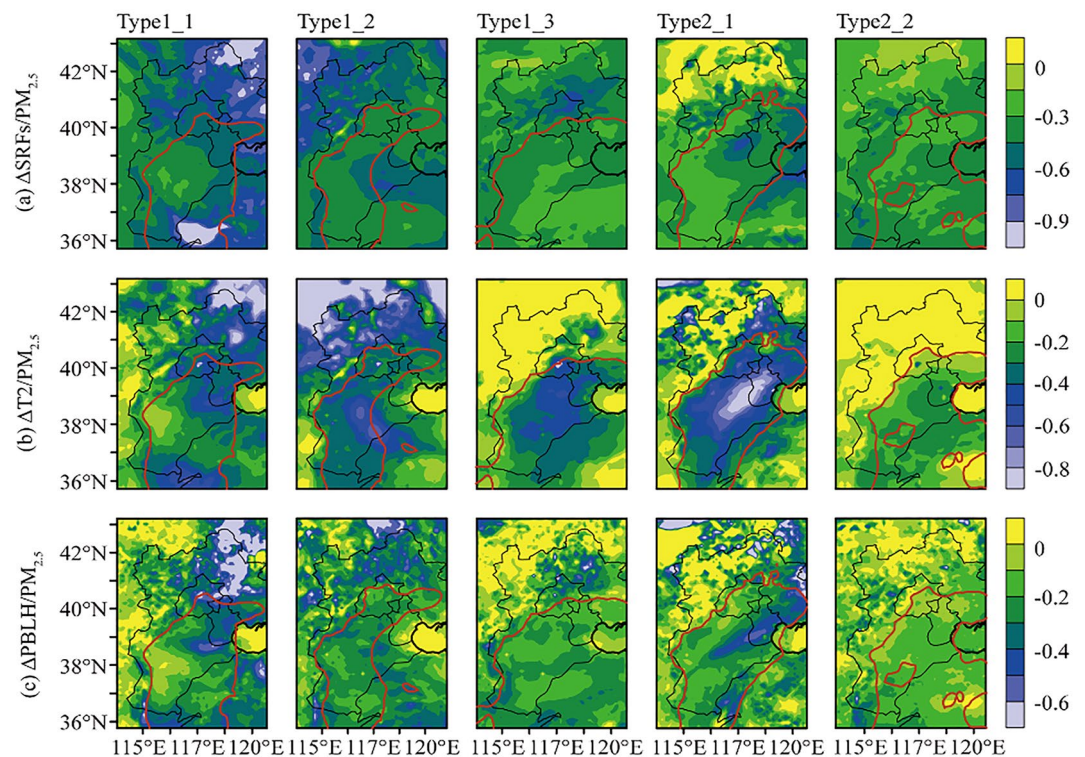
Figure 10. The changes in (a) shortwave radiative flux at the surface (ΔSRFs; W m^{-2}), (b) 2-m temperature (ΔT2; °C), (c) planetary boundary layer height (ΔPBLH; m) caused by aerosol direct radiative effects (CTRL minus NODIR) divide by surface-layer PM$_{2.5}$ concentrations from the CTRL simulation for the five cases. All the panels were the averages over each event. The red lines indicate the areas in North China Plain with PM$_{2.5}$ concentrations >150 μg m^{-3}.

5.3. Simulated Changes in Winds

Figure 11 shows for each case the wind and GHT at 500 hPa, wind and GHT at 850 hPa, 10-m wind and SLP, as well as the vertical velocity from the CTRL simulation. At 500 hPa, the westerlies prevailed in Type1_2 and Type1_3, and the northwesteries prevailed in Type1_1, Type2_1, and Type2_2. These winds were consistent with the general situation that the 500 hPa GHT was high in the southwestern China (Northern Sichuan province and eastern Qinghai province) and low in the northeastern China (Liaoning province and southern Jilin province). At 850 hPa, the NCP region was dominated by westerlies in Type1_2, Type1_3, and Type2_2, northwestlies in Type1_1, and southwestlies in Type2_1. It is worth noting that an anti-cyclone occurred at 850 hPa in all cases (indicated by blue arrows in the second row of Figure 11). The anti-cyclone occurred in the south of NCP in Type1_2, Type1_3, and Type2_2, in the southwest of NCP in Type1_1, and in the southeast of NCP in Type2_1. The position of this anti-cyclone determined the wind direction in the NCP region. At 10-m altitude, an anti-cyclone occurred in the southeast of NCP in Type1_1, Type1_2, and Type2_2 because of the high SLP in that region, and an anti-cyclone occurred over NCP in Type1_3 and Type2_1 owing to a weak high center of SLP located over NCP or east of NCP.

Figure 11 also shows the vertical cross sections of vertical velocity averaged over the latitudes of 27.5–48.0°N. A downward flow occurred over NCP in all cases. Such general downward flow agrees with the schematic circulation pattern for the formation of severe haze events in North China, as summarized by Liao, Sun et al. (2015), Wu et al. (2017), and Ding et al. (2017). The downdraft between 700 hPa and 900 hPa restrains the development of the boundary layer and leads to the continuous accumulation of pollutants in the lower boundary layer.

Figure 12 shows the same meteorological fields as in Figure 11 but are the changes caused by aerosol DRE (CTRL-NODIR). At 500 hPa, an anti-cyclone caused by aerosol DRE around NCP was found in all the cases, which was consistent with the increases in GHT in the east of NCP by aerosol DRE. Type1_2, Type2_1, and
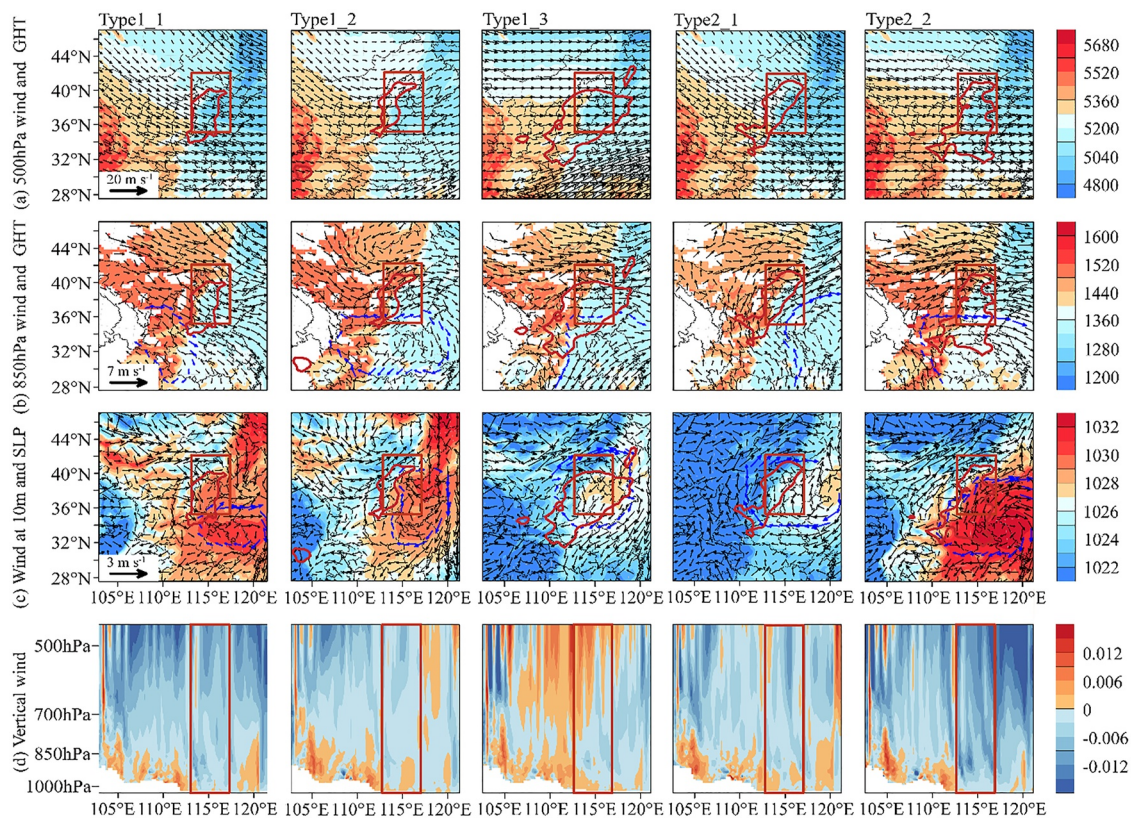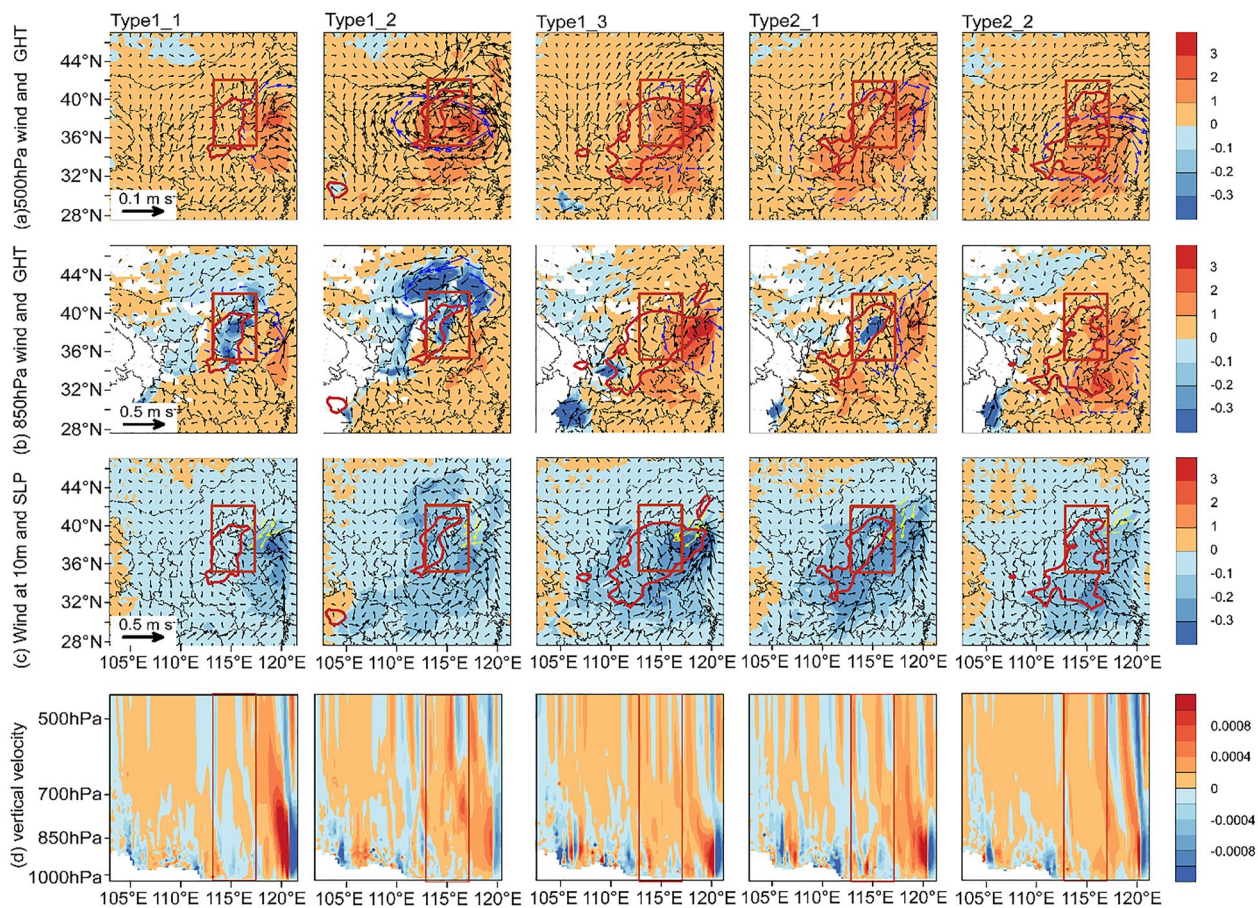
Figure 11. Spatial distributions of (a) wind and geopotential height (m) at 500 hPa, (b) wind and geopotential height at 850 hPa, (c) 10-m wind and sea level pressure (SLP) (hPa), as well as (d) the cross sections of vertical velocity (m s⁻¹) (positive value means upward flow and negative value denotes downward flow) from the CTRL simulation. The blue arrows in (b and c) indicate cyclones or anticyclones. The red rectangles indicate the North China Plain region and the red lines indicate the areas with PM$_{2.5}$ concentration >150 µg m⁻³. The cross sections were averaged over the latitudes of 27.5–48.0°N. All the panels were averaged over each event.

Type2_2 had the anti-cyclone in the south of NCP, and the rest cases had the anti-cyclone in the east of NCP. At 850 hPa, the changes in GHT caused by aerosol DRE over or near NCP were either positive or negative, which were determined by aerosol-induced changes in temperature at 850 hPa (Figure S4a in Supporting Information S1). Over the locations with the decreases (increases) in temperature, the GHT decreased (increased). The increases in GHT led to an anti-cyclone in the east of NCP in Type1_3 and in the south of NCP in Type2_2, and the decreases led to a cyclone near NCP in Type1_1 and in the north of NCP in Type1_2. At 10-m, there were common features in SLP and winds. Aerosol DRE reduced SLP over eastern China and led to anomalous northerlies and northeasterlies in the eastern or northeastern NCP. The reason of anomalous northerlies at the surface is that BC induces a strong warming in eastern NCP and hence an anomalous low pressure in NCP. The similar changes were also reported in Gao et al. (2016), Qiu et al. (2017), and Chen et al. (2022).

Vertically, an anomalous upward flow was caused by aerosol DRE from 850 hPa to 500 hPa in the NCP region (Figure 12), which weakened the downward flow in the CTRL simulation (Figure 11). This upward flow was caused by the increase in temperature at 850 hPa (Figure S4b in Supporting Information S1), resulting in thermal expansion of air and the rise of hot air.

6. Conclusions

This work quantifies the effects of aerosol DRE on meteorological variables during severe haze events by using the WRF-Chem model. Five heavily polluted events (15–17 January 2014, 13–15 January 2015, 8–10 December 2015, 21–23 December 2015, and 29–31 December 2016) in NCP were selected, aiming to obtain common characteristics among episodes. Three of the selected episodes belongs to the most dominant weather pattern for SPPDs and the rest episodes belong to the second most dominant weather pattern. As classified by Li et al. (2019), these two weather patterns in NCP were responsible for 35.7% and 31.2% of observed SPPDs,

Figure 12. (a) The changes in wind (m s^{-1}) and geopotential height (gpm) at 500 hPa, (b) wind and geopotential height at 850 hPa, (c) 10-m wind and sea level pressure (SLP) (hPa), as well as (d) the cross sections of vertical velocity (m s^{-1}). The blue arrows in (a and b) denote cyclones or anticyclones, yellow arrows in (c) indicate the abnormal northeasterlies. The red rectangles indicate the North China Plain region and the red lines indicate the areas with PM$_{2.5}$ > 150 μg m^{-3}. The cross sections were averaged over the latitude of 27.5–48.0°N. All the panels were averaged over each event.

respectively. Model evaluation showed that the WRF-Chem model can capture the temporal variations and spatial distributions of PM$_{2.5}$ but underestimates PM$_{2.5}$ concentrations with NMBs of −9.3% to −34.8% for the five cases. The model also reproduced fairly well the meteorological parameters including T2, RH2, 10-m wind speed and wind direction, as well as daily mean total radiation (shortwave plus longwave).

In the five cases mentioned above, averaged over the areas with PM$_{2.5}$ > 150 μg m^{-3} and over the event, simulated PM$_{2.5}$ concentrations reached 197.3, 187.0, 291.9, 215.8, 178.1 μg m^{-3}, which caused the decreases in net shortwave radiative flux by 86.7, 70.0, 85.8, 68.1, and 52.1 W m^{-2} at the surface and the reductions in T2 by 0.63, 0.67, 0.81, 0.97, and 0.28°C, respectively. Considering the changes in net shortwave radiative flux at the surface (ΔSRFs) and in boundary layer height (ΔPBLH) per unit mass of PM$_{2.5}$, the values were −0.46, −0.40, −0.31, −0.34, −0.31 W m^{-1} and −0.26, −0.24, −0.20, −0.24, −0.13 m^4 μg^{-1}, respectively, when averaged over the areas with surface-layer PM$_{2.5}$ > 150 μg m^{-3} and over the event.

Common features of aerosol-induced changes in temperature were found from the selected events. With aerosol DREs, temperatures were generally reduced at the surface and increased around 850 hPa. Considering the changes in temperature per unit mass of PM$_{2.5}$, values of ΔT2/PM$_{2.5}$ averaged over the region with PM$_{2.5}$ > 150 μg m^{-3} were −0.33, −0.36, −0.26, −0.44, −0.16 °C m^3 μg^{-1} 10^{-2} in the five cases, respectively. The largest ΔT2 did not always correspond to the highest PM$_{2.5}$ concentrations. The magnitudes of aerosol induced ΔT2 were also determined by winds (wind speed, wind direction, as well as the convergence or divergence of winds). While high wind speed could dilute the aerosol-induced cooling, the convergence of wind could limit the temperature change to local area. The surface cooling was also found to be associated with intrusion of cold air mass at 10-m altitude.
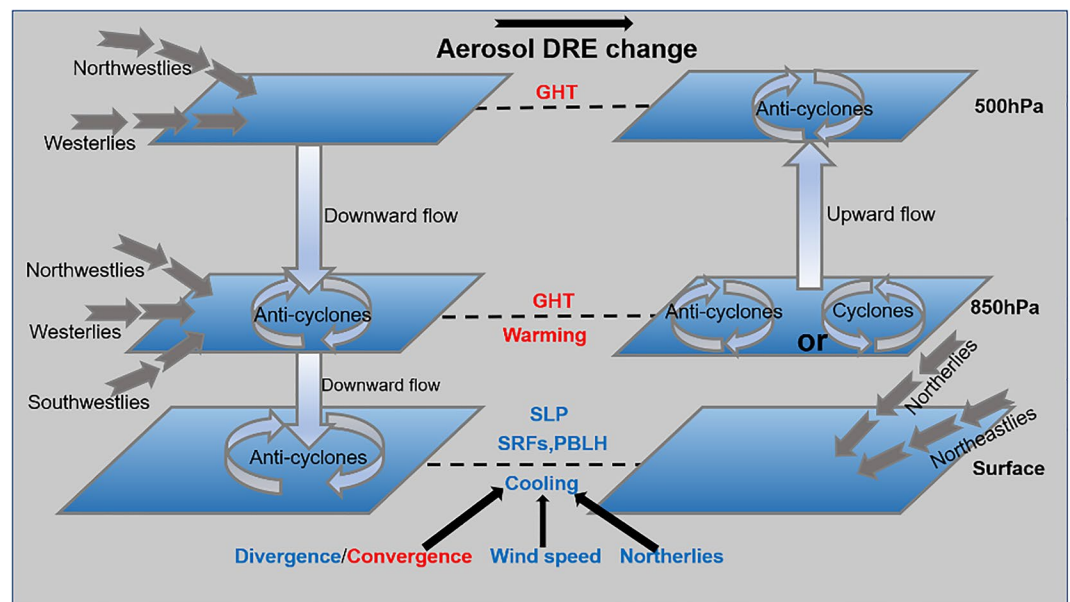
Figure 13. A schematic diagram of simulated winds and the changes in winds by aerosol direct radiative effects (DRE).

For example, the case of Type2_1 (21–23 December 2015) had the most intense northerlies on the third day of the event, which led to the largest negative $\Delta T2/PM_{2.5}$ among all the cases.

Common features of aerosol-induced changes in wind were also found from the selected events, as summarized in Figure 13. Aerosols induced an anti-cyclone at 500 hPa around NCP in all the cases, which was associated with the increases in GHT. At 850 hPa, the changes in GHT were consistent with the aerosol-induced changes in temperature (increases in temperature increase GHT and vice versa), which would cause either a cyclone or an anti-cyclone. At 10-m, aerosol DRE reduced SLP over eastern China and led to anomalous northerlies and north-easterlies in the east and northeast of NCP. Vertically, aerosol-induced an upward flow from 850 hPa to 500 hPa in the NCP region, which weakened the downward flow in the CTRL simulations.

Data Availability Statement

The observed meteorological datasets are publicly available from NOAA's National Climatic Data Center at http://gis.ncdc.noaa.gov/maps/ncei/cdo/hourly. The daily surface total radiation is obtained from China Meteorological Data Service Center at http://data.cma.cn. Hourly $PM_{2.5}$ datasets are collected from the China National Environmental Monitoring Center (CNEMC) (http://www.cnemc.cn). The Weather Research and Forecasting Model with online chemistry (WRF-Chem, version3.6) is a free-to-use community model (https://ruc.noaa.gov/wrf/wrf-chem/). The authors used the Multi-resolution Emission Inventory of China (MEIC) in the model for anthropogenic emissions (http://www.meicmodel.org). The authors used the WRF-Chem preprocessor tools mozbc, fire_emiss, anthro_emiss, and bio_emiss, available from the Atmospheric Chemistry Observations & Modeling website (https://www2.acom.ucar.edu/wrf-chem/wrf-chem-tools-community). Use NCAR Command Language (NCL) version 6.3.0 for figures and analysis.

References

Bi, J., Huang, J., Hu, Z., Holben, B. N., & Guo, Z. (2014). Investigating the aerosol optical and radiative characteristics of heavy haze episodes in Beijing during January of 2013. *Journal of Geophysical Research: Atmospheres*, *119*(16), 9884–9900. https://doi.org/10.1002/2014jd021757

Cai, W., Li, K., Liao, H., Wang, H., & Wu, L. (2017). Weather conditions conducive to Beijing severe haze more frequent under climate change. *Nature Climate Change*, *7*(4), 257–262. https://doi.org/10.1038/nclimate3249

Che, H., Xia, X., Zhu, J., Li, Z., Dubovik, O., Holben, B., et al. (2014). Column aerosol optical properties and aerosol radiative forcing during a serious haze-fog month over North China Plain in 2013 based on ground-based sunphotometer measurements. *Atmospheric Chemistry and Physics*, *14*(4), 2125–2138. https://doi.org/10.5194/acp-14-2125-2014

Chen, D., Liao, H., Yang, Y., Chen, L., Zhao, D., & Ding, D. (2022). Simulated impacts of vertical distributions of black carbon aerosol on meteorology and $PM_{2.5}$ concentrations in Beijing during severe haze events. *Atmospheric Chemistry and Physics*, *22*(3), 1825–1844. https://doi.org/10.5194/acp-22-1825-2022

Chen, F., & Dudhia, J. (2001). Coupling an advanced land surface–hydrology model with the Penn state–NCAR MM5 modeling System. Part II: Preliminary model Validation. *Monthly Weather Review*, *129*(4), 587–604. https://doi.org/10.1175/1520-0493(2001)129<0587:Caalsh>2.0.Co;2

Chen, L., Zhu, J., Liao, H., Gao, Y., Qiu, Y., Zhang, M., et al. (2019). Assessing the formation and evolution mechanisms of severe haze pollution in the Beijing–Tianjin–Hebei region using process analysis. *Atmospheric Chemistry and Physics*, *19*(16), 10845–10864. https://doi.org/10.5194/acp-19-10845-2019

Chen, S.-H., & Sun, W.-Y. (2002). A One-dimensional time dependent cloud model. *Journal of the Meteorological Society of Japan*, *80*(1), 99–118. https://doi.org/10.2151/jmsj.80.99

Ding, A. J., Huang, X., Nie, W., Sun, J. N., Kerminen, V. M., Petäjä, T., et al. (2016). Enhanced haze pollution by black carbon in megacities in China. *Geophysical Research Letters*, *43*(6), 2873–2879. https://doi.org/10.1002/2016gl067745

Ding, Y., Wu, P., Liu, Y., & Song, Y. (2017). Environmental and dynamic conditions for the occurrence of persistent haze events in north China. *Engineering*, *3*(2), 266–271. https://doi.org/10.1016/j.Eng.2017.01.009

Emmons, L. K., Walters, S., Hess, P. G., Lamarque, J. F., Pfister, G. G., Fillmore, D., et al. (2010). Description and evaluation of the model for ozone and related chemical tracers, version 4 (MOZART-4). *Geoscientific Model Development*, *3*(1), 43–67. https://doi.org/10.5194/gmd-3-43-2010

Gao, M., Carmichael, G. R., Wang, Y., Saide, P. E., Yu, M., Xin, J., et al. (2016). Modeling study of the 2010 regional haze event in the North China Plain. *Atmospheric Chemistry and Physics*, *16*(3), 1673–1691. https://doi.org/10.5194/acp-16-1673-2016

Gao, M., Han, Z., Tao, Z., Li, J., Kang, J.-E., Huang, K., et al. (2020). Air quality and climate change, topic 3 of the model inter-comparison study for Asia phase III (MICS-Asia III)—Part 2: Aerosol radiative effects and aerosol feedbacks. *Atmospheric Chemistry and Physics*, *20*(2), 1147–1161. https://doi.org/10.5194/acp-20-1147-2020

Gao, M., Yang, Y., Liao, H., Zhu, B., Zhang, Y., Liu, Z., et al. (2021). Reduced light absorption of black carbon (BC) and its influence on BC-boundary-layer interactions during "APEC Blue". *Atmospheric Chemistry and Physics*, *21*(14), 11405–11421. https://doi.org/10.5194/acp-21-11405-2021

Gao, Y., Zhang, M., Liu, Z., Wang, L., Wang, P., Xia, X., et al. (2015). Modeling the feedback between aerosol and meteorological variables in the atmospheric boundary layer during a severe fog–haze event over the North China Plain. *Atmospheric Chemistry and Physics*, *11*(8), 4279–4295. https://doi.org/10.5194/acp-15-4279-2015

Grell, G. A., & Freitas, S. R. (2014). A scale and aerosol aware stochastic convective parameterization for weather and air quality modeling. *Atmospheric Chemistry and Physics*, *14*(10), 5233–5250. https://doi.org/10.5194/acp-14-5233-2014

Guenther, A., Karl, T., Harley, P., Wiedinmyer, C., Palmer, P. I., & Geron, C. (2006). Estimates of global terrestrial isoprene emissions using MEGAN (model of emissions of gases and aerosols from nature). *Atmospheric Chemistry and Physics Discussions*, *6*(1), 107–173. https://doi.org/10.5194/acpd-6-107-2006

Hong, S. Y., Noh, Y., & Dudhia, J. (2006). A new vertical diffusion package with an explicit treatment of entrainment processes. *Monthly Weather Review*, *134*(9), 2318–2341. https://doi.org/10.1175/mwr3199.1

Hou, X., Zhu, B., Kumar, K. R., & Lu, W. (2019). Inter-annual variability in fine particulate matter pollution over China during 2013–2018: Role of meteorology. *Atmospheric Environment*, *214*, 116842. https://doi.org/10.1016/j.atmosenv.2019.116842

Li, J., Han, Z., Wu, Y., Xiong, Z., Xia, X., Li, J., et al. (2020). Aerosol radiative effects and feedbacks on boundary layer meteorology and $PM_{2.5}$ chemical components during winter haze events over the Beijing-Tianjin-Hebei region. *Atmospheric Chemistry and Physics*, *20*(14), 8659–8690. https://doi.org/10.5194/acp-20-8659-2020

Li, J., Liao, H., Hu, J., & Li, N. (2019). Severe particulate pollution days in China during 2013–2018 and the associated typical weather patterns in Beijing-Tianjin-Hebei and the Yangtze River Delta regions. *Environmental Pollution*, *248*, 74–81. https://doi.org/10.1016/j.envpol.2019.01.124

Li, K., Jacob, D. J., Liao, H., Qiu, Y., Shen, L., Zhai, S., et al. (2021). Ozone pollution in the North China plain spreading into the late-winter haze season. *Proceedings of the National Academy of Sciences of the United States of America*, *118*(10). https://doi.org/10.1073/pnas.2015797118

Liao, L., Lou, S., Fu, Y., Cang, W., & Liao, H. (2015). Radiative forcing of aerosols and its impact on surface air temperature on synoptic scale in eastern China. *Chinese Journal of Atmospheric Sciences*, *39*(1), 68–82. https://doi.org/10.3878/j.issn.1006-9895.1402.13302

Liao, X. N., Sun, Z., Tang, Y., Pu, W., Li, Z., & Li, B. (2015). Meteorological mechanism for the formation of a serious pollution case in Beijing in the background of northerly flow at upper levels. *Environmental Science*, *36*(3), 801–808. https://doi.org/10.13227/j.hjkx.2015.03.007

Lin, Y. L., Farley, R. D., & Orville, H. D. (1983). Bulk parameterization of the snow field in a cloud model. *Journal of Climate and Applied Meteorology*, *22*(6), 1065–1092. https://doi.org/10.1175/1520-0450(1983)022<1065:Bpotsf>2.0.Co;2

Liu, C., Gao, Z., Li, Y., Gao, C., Su, Z., & Zhang, X. (2019). Surface energy budget observed for winter wheat in the north China plain during a fog–haze event. *Boundary-Layer Meteorology*, *170*(3), 489–505. https://doi.org/10.1007/s10546-018-0407-x

Liu, Q., Jia, X., Quan, J., Li, J., Li, X., Wu, Y., et al. (2018). New positive feedback mechanism between boundary layer meteorology and secondary aerosol formation during severe haze events. *Scientific Reports*, *8*(1), 6095. https://doi.org/10.1038/s41598-018-24366-3

Qiu, Y., Liao, H., Zhang, R., & Hu, J. (2017). Simulated impacts of direct radiative effects of scattering and absorbing aerosols on surface layer aerosol concentrations in China during a heavily polluted event in February 2014. *Journal of Geophysical Research: Atmospheres*, *122*(11), 5955–5975. https://doi.org/10.1002/2016jd026309

Sha, T., Ma, X., Wang, J., Tian, R., Zhao, J., Cao, F., & Zhang, Y. L. (2022). Improvement of inorganic aerosol component in $PM_{2.5}$ by constraining aqueous-phase formation of sulfate in cloud with satellite retrievals: WRF-Chem simulations. *Science of the Total Environment*, *804*, 150229. https://doi.org/10.1016/j.scitotenv.2021.150229

Wang, T., Jiang, F., Deng, J., Shen, Y., Fu, Q., Wang, Q., et al. (2012). Urban air quality and regional haze weather forecast for Yangtze River Delta region. *Atmospheric Environment*, *58*, 70–83. https://doi.org/10.1016/j.atmosenv.2012.01.014

Wang, Y., Yao, L., Wang, L., Liu, Z., Ji, D., Tang, G., et al. (2013). Mechanism for the formation of the January 2013 heavy haze pollution episode over central and eastern China. *Science China Earth Sciences*, *57*(1), 14–25. https://doi.org/10.1007/s11430-013-4773-4

Wang, Z., Huang, X., & Ding, A. (2018). Dome effect of black carbon and its key influencing factors: A one-dimensional modelling study. *Atmospheric Chemistry and Physics*, *18*(4), 2821–2834. https://doi.org/10.5194/acp-18-2821-2018

Wen, W., Guo, C., Ma, X., Zhao, X., Liu, L., Chen, D., & Xu, J. (2020). Impact of emission reduction on aerosol-radiation interaction during heavy pollution periods over Beijing-Tianjin-Hebei region in China. *Journal of Environmental Sciences*, *95*, 2–13. https://doi.org/10.1016/j.jes.2020.03.025

Wiedinmyer, C., Akagi, S. K., Yokelson, R. J., Emmons, L. K., Al-Saadi, J. A., Orlando, J. J., & Soja, A. J. (2011). The fire INventory from NCAR (FINN): A high resolution global model to estimate the emissions from open burning. *Geoscientific Model Development*, *4*(3), 625–641. https://doi.org/10.5194/gmd-4-625-2011

Wild, O., Zhu, X., & Prather, M. J. (2000). Fast-J: Accurate simulation of in- and below-cloud photolysis in tropospheric chemical models. *Journal of Atmospheric Chemistry*, *37*(3), 245–282. https://doi.org/10.1023/a:1006415919030

Wu, J., Bei, N., Hu, B., Liu, S., Zhou, M., Wang, Q., et al. (2019). Aerosol–radiation feedback deteriorates the wintertime haze in the North China Plain. *Atmospheric Chemistry and Physics*, *19*(13), 8703–8719. https://doi.org/10.5194/acp-19-8703-2019

Wu, P., Ding, Y., & Liu, Y. (2017). Atmospheric circulation and dynamic mechanism for persistent haze events in the Beijing–Tianjin–Hebei region. *Advances in Atmospheric Sciences*, *34*(4), 429–440. https://doi.org/10.1007/s00376-016-6158-z

Xia, W., Wang, Y., Chen, S., Huang, J., Wang, B., Zhang, G. J., et al. (2022). Double trouble of air pollution by anthropogenic dust. *Environmental Science & Technology*, *56*(2), 761–769. https://doi.org/10.1021/acs.est.1c0477

Yu, X., Kumar, K. R., Lu, R., & Ma, J. (2016). Changes in column aerosol optical properties during extreme haze-fog episodes in January 2013 over urban Beijing. *Environmental Pollution*, *210*, 217–226. https://doi.org/10.1016/j.envpol.2015.12.021

Zaveri, R. A., Easter, R. C., Fast, J. D., & Peters, L. K. (2008). Model for simulating aerosol interactions and chemistry (MOSAIC). *Journal of Geophysical Research*, *113*(D13), D13204. https://doi.org/10.1029/2007jd008782

Zaveri, R. A., & Peters, L. K. (1999). A new lumped structure photochemical mechanism for large-scale applications. *Journal of Geophysical Research*, *104*(D23), 30387–30415. https://doi.org/10.1029/1999jd900876

Zhang, X., Zhang, Q., Hong, C., Zheng, Y., Geng, G., Tong, D., et al. (2018). Enhancement of $PM_{2.5}$ concentrations by aerosol-meteorology interactions over China. *Journal of Geophysical Research: Atmospheres*, *123*(2), 1179–1194. https://doi.org/10.1002/2017jd027524

Zhang, Y., Ding, A., Mao, H., Nie, W., Zhou, D., Liu, L., et al. (2016). Impact of synoptic weather patterns and inter-decadal climate variability on air quality in the North China Plain during 1980–2013. *Atmospheric Environment*, *124*, 119–128. https://doi.org/10.1016/j.atmosenv.2015.05.063

Zhao, C., Liu, X., Leung, L. R., Johnson, B., McFarlane, S. A., Gustafson, W. I., et al. (2010). The spatial distribution of mineral dust and its shortwave radiative forcing over north Africa: Modeling sensitivities to dust emissions and aerosol size treatments. *Atmospheric Chemistry and Physics*, *10*(18), 8821–8838. https://doi.org/10.5194/acp-10-8821-2010

Zheng, Y., Che, H., Xia, X., Wang, Y., Zhao, H., Wang, H., et al. (2017). A comparative analysis of aerosol microphysical, optical and radiative properties during the spring festival holiday over Beijing and surrounding regions. *Aerosol and Air Quality Research*, *18*(7), 1774–1787. https://doi.org/10.4209/aaqr.2017.10.0396

Zheng, Y., Che, H., Yang, L., Chen, J., Wang, Y., Xia, X., et al. (2017). Optical and radiative properties of aerosols during a severe haze episode over the North China Plain in December 2016. *Journal of Meteorological Research*, *31*(6), 1045–1061. https://doi.org/10.1007/s13351-017-7073-7